In situ study of the formation mechanism of two-dimensional superlattices from PbSe nanocrystals

In-situ study of consecutive phase transitions in the formation of atomically coherent two-dimensional superlattices from nanocrystals

Jaco J. Geuchies[1,5a†], Carlo van Overbeek[1†], Wiel H. Evers[2,3], Bart Goris[4], Annick de Backer[4], Anjan P. Gantapara[6], Freddy. T. Rabouw[1], Jan Hilhorst[5b], Joep L. Peters[1], Oleg Konovalov[5a], Andrei V. Petukhov[7,8], Marjolein Dijkstra[6], Laurens D.A. Siebbeles[2], Sandra van Aert[4], Sara Bals[4] and Daniel Vanmaekelbergh[1*]

[†] These authors contributed equally to this work

*Corresponding author: Prof. dr. Daniel Vanmaekelbergh. Email: d.vanmaekelbergh@uu.nl

1 Condensed Matter and Interfaces, Debye Institute for Nanomaterials Science, Utrecht University, The Netherlands

2. Optoelectronic Materials Section, Department of Chemical Engineering, Delft University of Technology, The Netherlands

3. Kavli Institute of Nanoscience, Delft University of Technology, The Netherlands

4. Electron Microscopy for Materials Science (EMAT), University of Antwerp, Belgium

5. [a]ID10/ [b]ID01, European Synchrotron Radiation Facility (ESRF), France

6. Soft Condensed Matter, Debye Institute for Nanomaterials Science, Utrecht University, The Netherlands

7. Physical and Colloidal Chemistry, Debye Institute for Nanomaterials Science, Utrecht University, The Netherlands

8. Laboratory of Physical Chemistry, Department of Chemical Engineering and Chemistry, Eindhoven University of Technology, The Netherlands

Oriented attachment of nanocubic PbSe building blocks can result in the formation of 2-D superstructures with long-range nanoscale and atomic order [1,2]. This questions the applicability of classic models in which the superlattice grows by first forming a nucleus, followed by sequential irreversible attachment of nanocrystals [3,4], since one "wrong" attachment would disrupt the 2-D order beyond repair. We have studied the mechanism of the formation of 2-D PbSe superstructures with square geometry using in-situ grazing-incidence X-ray scattering (small-angle and wide-angle), ex-situ electron microscopy, and Monte Carlo simulations. We observe nanocrystal adsorption at the liquid-gas interface, followed by the formation of a hexagonal nanocrystal monolayer. The hexagonal geometry transforms gradually through a pseudo-hexagonal phase into a phase with square order; simulations suggest that this phase transition is driven by attractive interactions between the {100} planes perpendicular to the liquid substrate that tend to maximize the facet-to-facet overlap. Finally, the nanocrystals attach atomically via a necking process, resulting in atomically coherent 2-D square superlattices.

Oriented atomic attachment of colloidal nanocrystals (NCs), i.e. the formation of a single crystal by atomic connection of smaller crystals, is an important process in geology [5-8], and recently gained much attention as a preparation tool in semiconductor nanoscience [9,10]. We reported a method to prepare 2-dimensional (2-D) atomically coherent PbSe superlattices, starting from a suspension of PbSe NCs [1,2]. The NCs have the shape of a truncated cube, consistent with the rock salt crystal structure of PbSe (see Fig. S1). A suspension of these NCs is cast onto a surface of an immiscible liquid, ethylene glycol, and the solvent is evaporated at room temperature. During the evaporation, extended sheets are formed with a thickness of one NC monolayer [1].

The 2-D structure shows a nanoscale geometry with square periodicity with, to some extent, also atomic coherency. In this so-called square geometry, all NCs are directed with a <100> axis perpendicular to the 2-D plane, and are laterally connected via the in-plane {100} facets. This means that two out of six {100} facets, namely those at the top and the bottom of the 2-D sheet, are not used for attachment.

Nanocrystal self-assembly and atomic attachment forms a unique route to prepare 2-D semiconductors with a superimposed geometry on the nanometer scale that influences the band structure and can result in semiconductors with Dirac-type valence and conduction bands and high charge carrier mobility [10-13,34]. Although superlattices with a square geometry are slightly disordered on the atomic scale, they show amazing long-range ordering on the nano-scale. A better understanding of the formation process is required for further progress in the synthesis of these systems. The 2-D long-range ordering cannot be explained in terms of the classic nucleation and growth model [3,4]. In this model the interactions between a crystal (nucleus) and building blocks are supposed to be relatively weak, in the order of a few k_BT. As a result, the building blocks can bind and unbind to an existing crystal, until the optimal binding geometry is found, resulting in ordering over long distances. In the case of superlattice formation by oriented attachment of NCs this mechanism cannot be operative, because per NC-NC connection, chemical bonds are formed between tens of atoms on opposing crystal facets. The corresponding energy change is orders of magnitude larger than the thermal energy, and oriented attachment should therefore be irreversible. Thus “incorrect” irreversible attachments should lead to disruption of the long-range nanoscale order in the superlattice.

Here, we present a real-time study of the growth of 2-D superlattices with a square periodicity. We monitor the reactive self-assembly in real time and in-situ by simultaneous grazing-incidence small-angle and wide-angle X-ray scattering (GISAXS and GIWAXS), see Fig. S1. Moreover, we scoop the structures formed at different stages of the process for analysis with ex-situ Transmission Electron Microscopy (TEM). Previous work on self-assembly of NCs has either focused on only monitoring the long-range order on the NC scale using GISAXS [14] or ex-situ measurements using GISAXS and GIWAXS [15-18], but a full time-resolved study of oriented attachment of NCs at the liquid-air interface on both nanocrystal and atomic length scales has not been performed. We find that oriented attachment of the nanocrystals by neck formation is preceded by a remarkable sequence of processes: nanocrystal adsorption at the liquid/air interface with the preservation of the rotational degrees of freedom, formation of a dense hexagonal NC phase, finally followed by a phase transition from hexagonal into square order in the NC monolayer in which the rotations become entirely frozen.

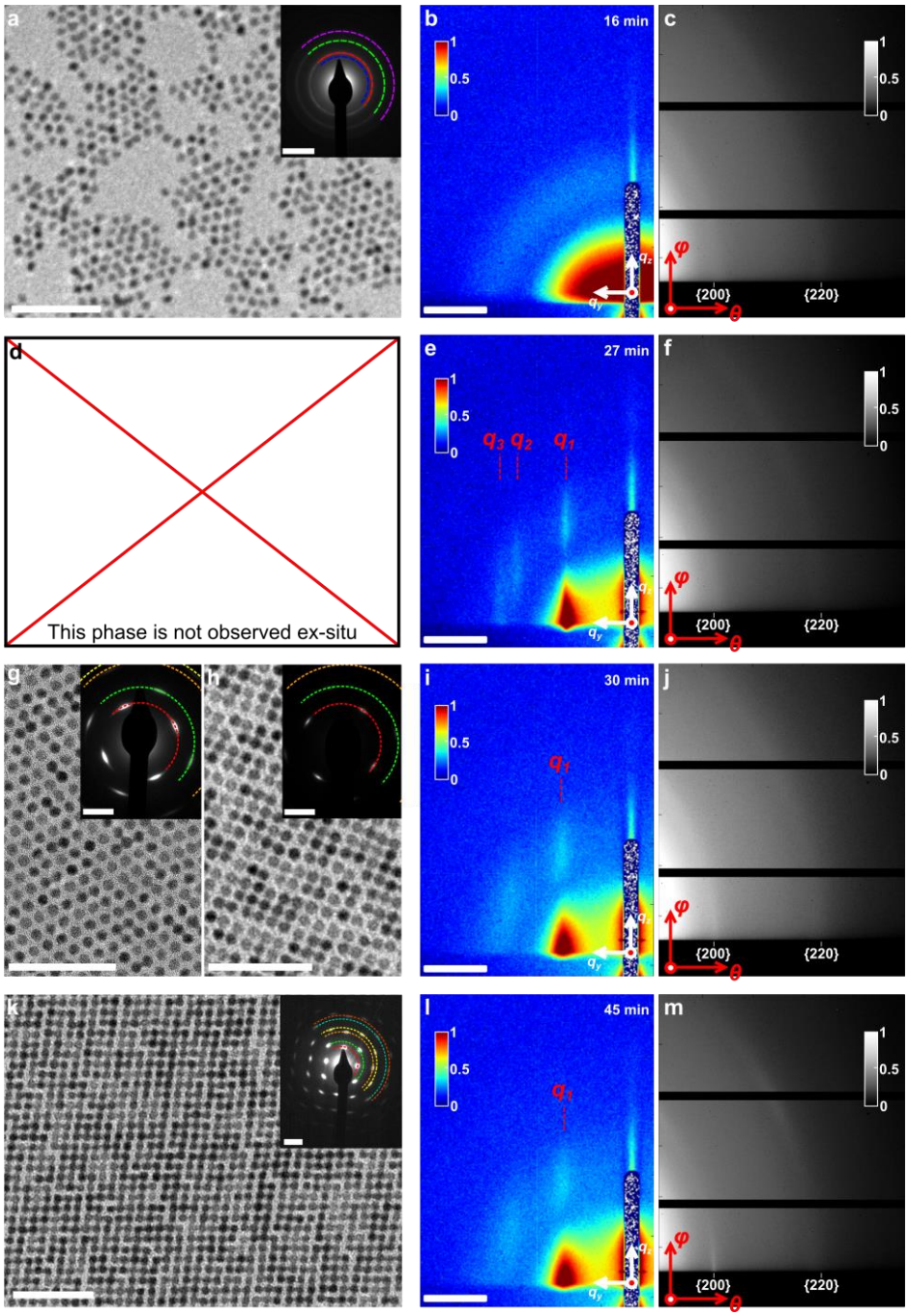

Figure 1: The different stages of the self-assembly process towards an oriented attached PbSe NC superlattice. *Ex-situ TEM images and in-situ X-ray scattering data are taken at different stages in the hexagonal-to-square phase transition. Top to bottom rows show the different phases over time.* ***(a)*** *TEM image of the disordered NCs, obtained by scooping immediately after drop casting on ethylene glycol. Inset shows the corresponding ED pattern, where diffraction rings indicate random orientations of the NCs, i.e. they have rotational freedom.* ***(b)*** *At the initial stage, we observe form factor scattering in GISAXS, indicating the presence of NCs without long-range positional order.* ***(c)*** *The GIWAXS pattern shows the full {200} and {220} diffraction rings of PbSe, indicating rotational freedom.* ***(d)*** *No hexagonal phase could be isolated ex-situ.* ***(e)*** *GISAXS pattern showing the presence of a hexagonal nanocrystal monolayer at the interface, with* ***(f)*** *the corresponding GIWAXS pattern.* ***(g)*** *TEM image of the pseudo-hexagonal phase, obtained when scooping the NCs just before toluene has completely evaporated. Inset: in ED the rings transformed into arcs.* ***(h)*** *TEM image of the initial square phase, before completely attachment of all NCs. Inset: the arcs in the ED have narrowed.* ***(i)*** *GISAXS pattern of*

the corresponding phase. Note that all peaks have broadened. ***(j)*** *GIWAXS pattern corresponding to* ***(i)****.* ***(k)*** *TEM image of the final square phase. Inset: the ED pattern now consists of distinct spots, at least up to the {600} reflection is visible.* ***(l)*** *GISAXS pattern of the final square phase, with* ***(m)*** *the corresponding GIWAXS pattern. Note how the diffraction rings have spots superimposed. The {200} diffraction has a narrower width in the 2θ-direction than before (compare j), indicating that the NCs have attached in this direction. All TEM scale bars correspond to 50 nm. The ED scale bars denote 20 nm^{-1}. The colored rings in the ED patterns display the position of the diffraction rings: blue = {111}, red = {200}, green = {220}, purple = {222}, orange = {400}, yellow = {420}, turquoise = {440}, brown = {600}. All GISAXS scale bars denote 1 nm^{-1}.*

In Fig. 1 we follow the formation of the square superlattice starting from individual NCs, combining ex-situ TEM and electron diffraction (ED) with in-situ GISAXS and GIWAXS. The TEM and X-ray scattering measurements show the same stage in the NC assembly process. However, TEM data should be handled with care as a structure extracted at a given time during the self-assembly process may undergo changes during drying.

In the initial stages of the self-assembly process (16 minutes after the start of solvent evaporation), it is not clear whether the NCs are still dispersed or already adsorbed at the toluene/air interface (Fig. 1(b,c)); but certain long-range positional order (Fig. 1(a,b)) or atomic orientation (Fig. 1(c)) is lacking.

After 27 minutes, diffraction rods appear in the GISAXS pattern (Fig. 1(e)), at scattering vectors of 0.80 nm^{-1}, 1.39 nm^{-1} and 1.61 nm^{-1}, consistent with a 2-D hexagonal structure at the liquid-gas interface (see Fig. S3). We were not able to isolate this structure ex-situ (Fig. 1(d)), demonstrating the importance of the in-situ scattering measurements. The corresponding GIWAXS pattern in Fig. 1(f) still shows the PbSe {200} and {220} diffraction rings, with no sign of a preferential crystallographic orientation or attachment of the NCs. At this stage we conclude that the NCs behave like hard spheres; the hexagonal packing is driven by entropy (presumably due to residual toluene, adding a repulsive contribution to the NC pair potential) and the NCs form a monolayer with the highest possible surface density [20].

At longer times, a complete monolayer of NCs is adsorbed at the interface. The NCs form a 2-D pseudo-hexagonal (PH) close-packed layer (Fig. 1(g)), with bond-angles deviating from the 60° of a perfect hexagonal structure. In the corresponding ED pattern the {111} and {222} rings are missing, meaning that all NCs have a {100} facet pointing upwards (see Fig. S4). Moreover, the ED pattern shows diffraction arcs rather than full rings, indicating that the NCs have a preferred crystallographic orientation in the 2-D plane. The width of the arcs reflects the remaining in-plane rotational freedom of the NCs. In the GISAXS pattern obtained 30 minutes after the start of the experiment (Fig. 1(i)) the first diffraction rod has moved further from the origin, indicating that the average NC–NC distance has decreased compared to Fig. 1(e). The diffraction peaks are broader than before, consistent with a peak splitting due to deviations of the superlattice symmetry from perfectly hexagonal (see Supplementary Methods 3). An alternative explanation for the broadening of the GISAXS reflections could be the increase of superlattice disorder due to evaporation of residual solvent [20,21]. However, we point out that we scooped a sample of this exact sample and confirmed the formation of the square superlattice (see figure S5), supporting the former interpretation of the scattering data. In the corresponding GIWAXS pattern (Fig. 1(j)) we observe the first indications of spots of increased intensity on the atomic diffraction rings, indicative for NC orientation with a <100> axis perpendicular to the liquid-gas interface. In Fig. 1(h) many NC–NC atomic connections have formed, but not yet all NCs make the maximum number of four NC–NC bonds with their in-plane {100} facets. The diffraction

arcs in the ED pattern have further narrowed, since the rotational freedom has decreased with respect to the PH phase of Fig. 1(g).

Finally, the NCs attain a square ordered structure (Fig. 1(k,l)) with the <100> direction pointing upward and orientational order in the 2-D plane (inset Fig. 1(k)). Furthermore, the NCs attach, as evidenced not only in the TEM image (Fig. 1(k)), but also from the narrowing of the {200} diffraction spot in the horizontal direction in the GIWAXS pattern (Fig. 1(m)). This is confirmed by later TEM measurements on the structure formed during the in-situ measurement (Fig. S5).

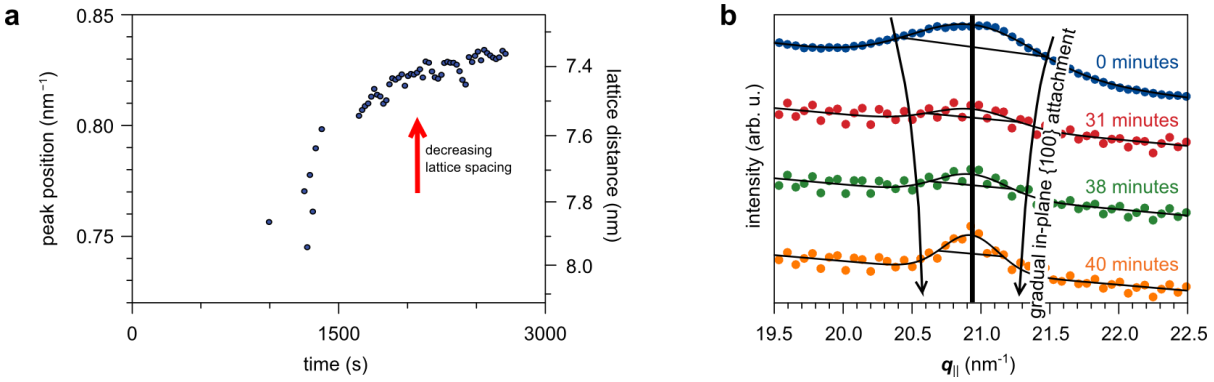

Figure 2: Quantitative analysis of the GISAXS and GIWAXS data. (a) *Fitted peak positions of the first diffraction rod q_1 in the horizontal scattering direction from the in-situ GISAXS measurements depicted in Fig. 1. From the position of the diffraction rod the lattice spacing is calculated.* ***(b)*** *Evolution of the peak width of the in-plane {200} atomic reflection in the horizontal scattering direction $\boldsymbol{q}_{||}$ over time as measured with GIWAXS. The black line is the calculated position of the {200} reflection for a rock salt PbSe crystal structure with a lattice vector of 6 Å.*

We now investigate in more detail the structural changes observed in the in-situ experiments. We calculate the time-evolution of the nanoscale lattice spacing from the position of the first diffraction rod in GISAXS (see Fig. 2(a)). The fitted peak position in reciprocal space (left axis) increases from 0.74 nm^{-1} to 0.83 nm^{-1}. Realizing that the initial structure has hexagonal symmetry while the final structure is square, this corresponds to a contraction of the NC-NC distance by 17%, from 9.1 nm after 1200 s after injection, to 7.6 nm at 2700 s (Fig. S3).

The initial NC–NC distance of 9.1 nm is as expected in a hexagonal monolayer of NCs of 5.7±0.6 nm core diameter separated by oleic acid ligands (roughly 2 nm in length). In the final oriented attached square structure, however, the NC–NC distance of 7.6 nm is 34% larger than the original PbSe NC core diameter. This shows that necking takes place during the atomic attachment, i.e. the formation of a crystal bridge between opposed {100} facets [2,5,24].

The increase of the average atomic coherence length during the formation can be extracted from the width of the horizontal atomic {200} reflections in GIWAXS (see Fig. 2(b)). The FWHM of the {200} peak of individual NCs in dispersion equals 1.1 nm^{-1}, corresponding to an average crystalline domain size of 5.9 nm, consistent with the NC sizes measured with TEM. During the in-situ experiments, the FWHM decreased to a value of 0.7 nm^{-1} after 31 minutes and 0.5 nm^{-1} after 40 minutes. These values correspond to crystalline domain sizes of 9.1 nm and 13.2 nm in the horizontal <100> direction. We conclude that when NCs attach atomically, the size of single-crystalline domains grows to on average to a lower limit of two to three NC diameters (see also Fig. S7), which agrees with the TEM sample obtained from the same experiment (Fig. S5).

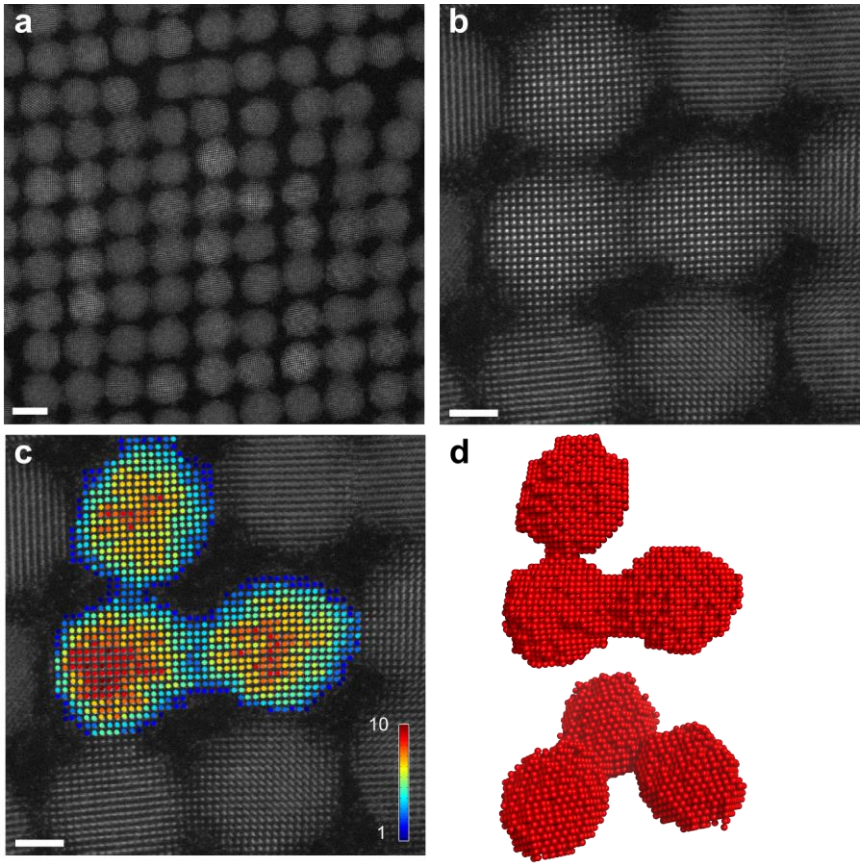

Figure 3: HAADF-STEM and atom counting reconstruction on the attached NCs. ***(a)*** *Typical overview HAADF-STEM image on a square superlattice.* ***(b)*** *More detailed HAADF-STEM image on NCs attached in a square superlattice, showing truly epitaxial connections and connections with crystal defects.* ***(c)*** *Results from the atom counting procedure, using (b) as an input image. The colorbar represents the number of detected atoms in the column.* ***(d)*** *Topview and sideview of the reconstructed atomic model. Scale bars equal 5 nm in* ***a*** *and 2 nm in* ***b*** *and* ***c****.*

In order to study the degree of atomic coherency inside the superlattice, we performed aberration corrected high angle annular dark field (HAADF) scanning transmission electron microscopy (STEM) measurements to investigate the atomic lattice. Fig. 3(a) shows a typical overview HAADF-STEM image of the square superlattice. When we acquire a more detailed image, Fig. 3(b), we observe atomic connections between the nanocrystals that are fully coherent, and some defective connections as well. In the supplementary information (Fig. S22) we show that these defective connections do not perturb the square periodicity of the superlattice which holds up to mesoscopic distances. From the HAADF-STEM image we extract the number of atoms in each projected atomic column using atom counting (Fig. 3(c)). [24,25] These numbers can then be used as an input for an iterative energy minimization scheme in order to obtain a 3D model for the investigated superlattice as illustrated in Figures 3(d). [26,27] More experimental details are provided in the Methods section and an additional example of two connected nanocrystals is presented in Fig. S23.

Combining all information from the in-situ and ex-situ experiments, we postulate a model for the reactive self-assembly of PbSe nanocubes into the square oriented attached superlattice.

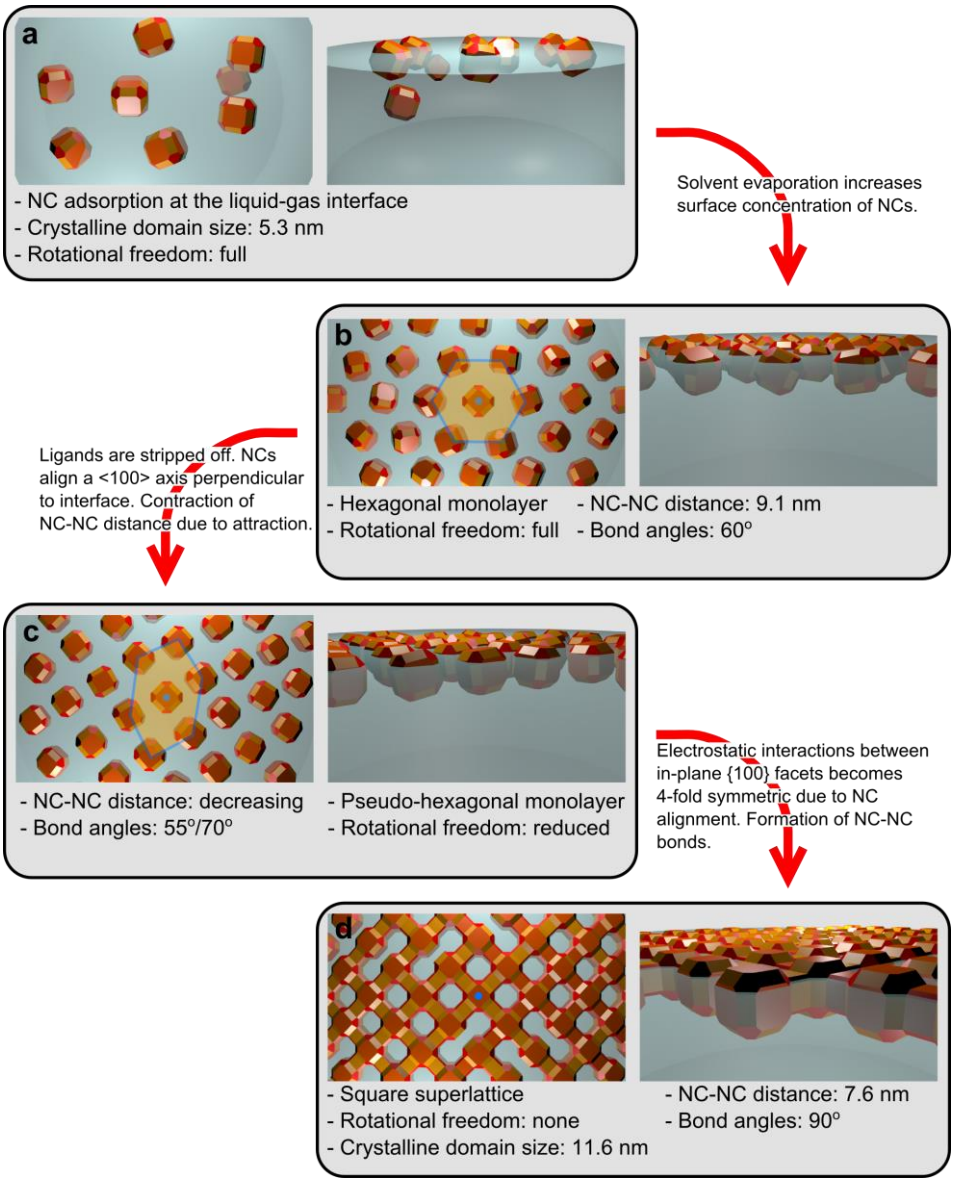

Figure 4: Schematic mechanism of the consecutive phase transitions during the reactive self-assembly of the PbSe NCs. *Left image shows top views, right image side views.* ***(a)*** *As the solvent evaporates, the concentration of the NCs increases, and the particles adsorb at the liquid-gas interface.* ***(b)*** *The central NC is indicated with a blue dot. The increase in NC concentration forces the particles to form a hexagonally packed monolayer.* ***(c)*** *The ligands on the {100} facets stabilizing the particles in the toluene slowly dissolve in the ethylene glycol substrate, thus increasing the {100} facet-to-facet attractive interaction and decreasing the NC-NC distance. Due to the directionality of the in-plane {100} attractions, the superlattice transforms into a pseudo-hexagonal structure.* ***(d)*** *Once the particles are sufficiently close, they connect atomically via necks; the superlattice obtains a square geometry.*

Fig. 4 shows cartoons of the different phases occurring in the reactive self-assembly. For clarity we omitted the oleic acid ligands from the image. During the toluene evaporation the NCs adsorb at the liquid-gas interface without long-range order (a). As the NC concentration at the interface increases, they start to form a hexagonally packed monolayer at the interface (b). The NCs still behave similar to hard spheres, as any anisotropic interaction is screened by the oleate ligands. Possibly, oleate ligands

weakly attached to the {100} facets [23], detach and are absorbed in the ethylene glycol phase. The particles align one of their <100> directions perpendicular to the liquid-gas surface. The rotational freedom in plane is gradually reduced, in favor of electrostatic and van der Waals interactions between opposed {100} facets. This also results in a reduced NC–NC distance (c). Due to the directionality of these in-plane {100} attractions, the superlattice has to change its symmetry from hexagonal to square. Once the NCs are in close proximity, crystalline bridges grow between neighboring NCs (d). This necking has also been observed in a chemically distinct case of NC attachment [8,28-30].

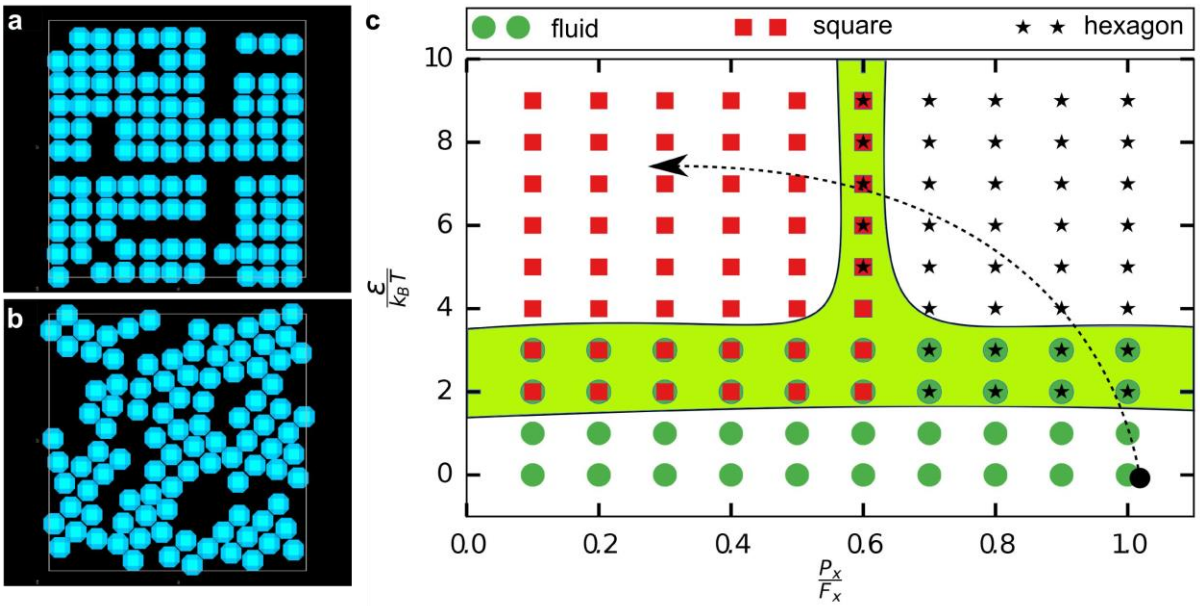

Figure 5: Monte-Carlo simulations on the truncated nanocubes confined to a 2D plane. ***(a)*** *Square phase (P_x/F_x = 0.1, ε/k_BT = 6) and* ***(b)*** *hexagonal/PH phase (P_x/F_x = 0.8, ε/k_BT = 6) obtained for different sizes of the attractive patches on the {100} facets.* ***(c)*** *State diagram for the truncated cubes with attractive {100} facets as a function of the relative attractive patch size on a {100} facet P_x/F_x, and the square-well interaction strength ε/k_BT between the attractive patches. The arrow depicts a possible route that describes the different phases observed in our experiments. The green shaded area shows regions where multiple phases coexist.*

To test the postulated model, we investigated the formation of superlattices from PbSe NCs adsorbed at the liquid-gas interface using Monte Carlo simulations with periodic boundary conditions in the canonical ensemble, i.e., we fixed the number of particles *N*, the volume *V*, and the temperature *T* of the system. We model the NCs by truncated cubes as depicted in Fig. S9. The cubes are confined to a 2D plane and are oriented such that the {100} facet points upwards. The nanocrystals are allowed to move freely in this plane. In the SI we calculate the interaction potential between two nanocrystals, which is the sum of the electrostatic and London interactions between all the atoms of the nanocrystals (see Supplementary Methods 7). The ligand-free {100} facets lead to an attractive driving force that attempts to position the nanocrystals with their vertical {100} facets face-to-face (see Fig. S24). This directional driving force is mimicked in the simulations by introducing small patches on the center of the vertical {100} facets. We assume the cantellated cubes to interact as hard particles, but with the attractive patchy interaction between the {100} facets. The patchy interaction is modelled as a square patch that interacts with an attractive square-well potential [31,32]. The patch size is defined by the ratio of the length of the patch P_x and the length of the {100} facet F_x, i.e., P_x/F_x, and the attraction strength is given by ε/k_BT with k_B Boltzmann's constant. We simulate the self-assembled

structures of the NCs as a function of the size of the attractive patch and the attraction strength in order to shed light on the contraction and symmetry change of the hexagonally packed layer towards the square superlattice, as shown in Fig. 1(g) to 1(k) and Fig. 4.

In Fig. 5(a) and 5(b), we show two typical configurations of the self-assembled structures for the cantellated cubes with different patch size. We clearly find that the self-assembled structure depends sensitively on the patch size, which determines the directionality of the attractive interaction. For a stronger directionality, i.e. smaller patch size, we observe a square symmetry for the superlattice (see Fig. 5(a)) whereas for a less directional interaction, i.e. a larger patch size, the superlattice shows hexagonal symmetry (see Fig. 5(b)). In Fig. 5(c) we present the state diagram of the nanocrystals as a function of the patch size P_x/F_x , and attraction strength ε/k_BT. We observe that the particles self-assemble into a superlattice for attraction strengths > $4\ k_BT$, even with very small attractive patch sizes. (see also Supplementary Methods 7). Our results corroborate our interpretation of the experimental data that the directional electrostatic and van der Waals interactions between the vertical {100} facets drive the phase transition from hexagonal to square NC ordering and keep the {100} facets face-to-face, finally enabling an atomic necking process and growth of attached nanocrystals that form single crystalline domains.

In summary, we have shown that the formation of 2-D nanoperiodic superlattices with a square symmetry from colloidal nanocrystals can be described by a sequence of processes, rather than oriented attachment alone. Following the temporal evolution of the superlattice formation by ex-situ TEM and in-situ X-ray scattering shows that the nanocrystals attach to the liquid-gas interface and form a hexagonally packed layer, which then contracts and transforms through a pseudo-hexagonal structure into a structure with square symmetry. During this phase transition, the NCs align themselves atomically and finally form inter-particle bonds. Monte Carlo simulations show that a directed attractive electrostatic and van der Waals interactions between in-plane {100} facets induce the (pseudo)-hexagonal to square phase transition.

[METHODS]

Nanocrystal synthesis

The PbSe nanocrystals used for the oriented attachment experiments in this study were prepared using the method described by Steckel et al. [33]. The synthesis was performed in a glovebox with a water and oxygen free environment. (a) 4.77g of lead acetate trihydrate (99.999% Aldrich), 10.35g of oleic acid (OA, 90% Aldrich) and 39.75g octadecene (ODE, 90% Aldrich) were heated to 130^{o}C under low pressure (10^{-3} bar) for approximately 4 hours. (b) A second mixture containing 3.52g Se (99.999% Alfa Aesar), 46.59 mL trioctylphosphine (TOP, 90% Fluka) and 0.41mL diphenylphosphine (DPP, 98% Aldrich) was prepared by dissolving the Se. Subsequently solution (a) was heated in a three-necked round-bottom flaks to 180^{o}C after which 15mL of solution (b) was rapidly injected. The particles were grown for approximately 60 seconds, after which the reaction was quenched with 20mL butanol. After the solution was cooled down to approximately 50^{o}C, 10 mL methanol was added to induce precipitation of the nanocrystals. The resulting suspension was centrifuged at 2500 rpm for 10 minutes, the supernatant was removed and the washed particles were redispersed in toluene. This washing procedure was repeated two times.

Oriented attachment of truncated PbSe nanocubes

The ex-situ oriented attachment was performed at 20°C inside a glovebox with <1ppm O_2 and <1ppm H_2O. A glass petri dish (Ø 27mm) was filled with 6.5 mL ethylene glycol. The nanocrystal (NC) solution with an initial concentration of $3.0x10^{-5}$mol/L was diluted by adding 4µL of the NC solution to 800µL of toluene. A total volume of 350µL of this dispersion was drop cast gently on top of the ethylene glycol. The ethylene glycol serves as an immiscible liquid substrate for the NC solution. After drying the NC solution on top of the EG for 60 minutes, a sample was scooped from the ethylene glycol interface on a copper TEM grid and dried in vacuum to remove any residual ethylene glycol.

In-situ GISAXS/WAXS

The in-situ X-ray scattering experiments under grazing incidence were performed at beamline ID10 of the European Synchrotron Radiation Facility (ESRF), Grenoble. The energy of the incident X-ray beam was set at 10.0 keV, below the Pb and Se absorption edges to minimize beam damage. We optimized the grazing angle to 0.3° for the best signal-to-noise ratio on both GIWAXS and GIWAXS detectors. The scattering was recorded by two Pilatus detectors. The GIWAXS patterns were recorded on a Pilatus 300K detector with 619x487 pixels, each 172x172µm^2 in size, positioned approximately 25 cm from the sample. The GISAXS patterns were recorded on a Pilatus 300K-W detector with 1475x195 pixels, each 172x172µm^2 in size, positioned 0.578 m from the sample. Before drop casting the dispersion of NCs on top of the EG substrate, the x-ray beam was aligned to the surface. After drop casting and every three minutes the alignment was repeated in <10 sec to adjust for solvent evaporation.

The oriented attachment was performed in a home-built liquid cell, which can be flushed with argon repeatedly to lower the oxygen and water levels (Fig. S10). A Teflon petri dish (Ø 64 mm) was filled with 28 mL of ethylene glycol. To the ethylene glycol we added 10 µL of an OA solution (1% (v/v) OA in ethylene glycol). The cell was then flushed five times with vacuum/argon cycles, and was filled with toluene saturated vapour (argon gas blown through hot toluene). Next, the PbSe NC solution (0.5 mL; $1.9x10^{-6}$ mol/L) was deposited on top of the liquid substrate.

As the PbSe NCs proved to be sensitive to beam damage, we scanned the sample position in between the measurement, back and forth over a distance of 4 mm (in 21 steps) in the direction perpendicular to the incident X-ray beam. In this way, the dose of X-ray photons on each position of the sample was minimized. Each frame was recorded with a 10 s integration time, after which the position of the sample was changed. After each sequence of 21 positions, we returned to the starting position and repeated the procedure.

HAADF-STEM imaging and atom counting

HAADF-STEM imaging is performed using an aberration corrected FEI Titan microscope operated at 300 kV. By modelling images as a superposition of Gaussian functions located at the atomic columns, the volume under each peak can be estimated by fitting this model to the region of interest. These volumes are integrated intensities of electrons and thus correspond to scattering cross-sections. In a subsequent analysis, the distribution of scattering cross-sections of all atomic columns is decomposed into overlapping normal distributions, where the number of normal components is selected using an Integrated Classification Likelihood (ICL) approach [24,25]. Based on the analysis of the image shown in Fig. 3, 10 components have been retrieved illustrating the presence of 1 up to a maximum of 10 atoms in a column. The number of atoms in each projected atomic column is then obtained by assigning the component which generates the experimental scattering cross-section with the highest

probability. In this manner, a map reflecting the number of atoms in each column is retrieved as illustrated in Fig. 3b.

Based on the counting results, a starting 3D configuration is obtained by positioning all Pb atoms on a perfect crystal grid symmetrically arranged around a central plane. Next, the potential energy of this configuration is calculated using a Lennard-Jones potential and minimized using an iterative scheme. In each iteration step, one atomic column, selected by a monte-carlo based approach, is shifted over one unit cell and the total energy is again calculated. The previous 3D configuration is replaced by the new one if the total energy is decreased. This procedure is repeated until convergence is reached.

[ACKNOWLEDGEMENTS]
This research is part of the program "Designing Dirac Carriers in semiconductor honeycomb superlattices (DDC)," which is supported by the Foundation for Fundamental Research on Matter (FOM), which is part of the Dutch Research Council (NWO). JJG acknowledges funding from the Debye and ESRF Graduate Programs. The authors gratefully acknowledge funding from the Research Foundation Flanders (G.036915 G.037413 and funding of postdoctoral grants to B.G. and A.D.B). S.B. acknowledges the European Research Council, ERC grant N°335078 – Colouratom. The authors gratefully acknowledge dr. Ingmar Swart for fruitful discussions.

The X-ray scattering measurements were performed at the ID10 beamline at ESRF under proposal numbers SC-4125 and SC-3786. The authors thank Giovanni Li Destri and Federico Zontone for their support during the experiments.

[AUTHOR CONTRIBUTIONS]
JJG, CVO, FTR, JH and JLP performed the in-situ GISAXS/WAXS experiments under supervision of OK and AVP. JJG and CVO analysed the GISAXS/WAXS data. The TEM data was collected by CVO, WHE, JJG and JLP. HAADF-STEM and atomic reconstructions were performed by BG, ADB, SVA and SB. APG and MD performed the Monte Carlo simulations. JJG and CVO wrote the manuscript under supervision of OK, AVP, MD, SB, LDAS and DV. DV supervised the whole project. The manuscript was written through contributions of all authors. All authors have given approval to the final version of the manuscript.

[COMPETING FINANCIAL INTERESTS]
The authors declare no competing financial interests

[ASSOCIATED CONTENT]
Supplementary information is available in the online version of the paper. Reprints and permissions information is available online at www.nature.com/reprints. Correspondence and requests for materials should be addressed to DV.

[REFERENCES]

1. Evers, W. H. *et al.* Low-dimensional semiconductor superlattices formed by geometric control over nanocrystal attachment. *Nano Lett.* **13**, 2317–2323 (2013).

2. Boneschanscher, M. P. *et al.* Long-range orientation and atomic attachment of nanocrystals in 2D honeycomb superlattices. *Science* **344**, 1377-1380 (2014). doi:10.1126/science.1252642

3. Pound, G. M. & Mer, V. K. La. Kinetics of Crystalline Nucleus Formation in Supercooled Liquid Tin 1,2. *J. Am. Chem. Soc.* **74**, 2323–2332 (1952).

4. LaMer, V. K. & Dinegar, R. H. Theory, Production and Mechanism of Formation of Monodispersed Hydrosols. *J. Am. Chem. Soc.* **72,** 4847–4854 (1950).

5. Banfield, J. F. Aggregation-Based Crystal Growth and Microstructure Development in Natural Iron Oxyhydroxide Biomineralization Products. *Science* **289**, 751–754 (2000).

6. Pacholski, C., Kornowski, A. & Weller, H. Self-assembly of ZnO: from nanodots to nanorods. *Angew. Chem. Int. Ed. Engl.* **41**, 1188–1191 (2002).

7. Li, D. *et al.* Direction-specific interactions control crystal growth by oriented attachment. *Science* **336**, 1014–1018 (2012).

8. Schliehe, C. *et al.* Ultrathin PbS sheets by two-dimensional oriented attachment. *Science* **329**, 550–553 (2010).

9. Cho, K.-S., Talapin, D. V, Gaschler, W. & Murray, C. B. Designing PbSe nanowires and nanorings through oriented attachment of nanoparticles. *J. Am. Chem. Soc.* **127**, 7140–7147 (2005).

10. Kalesaki, E., Evers, W. H., Allan, G., Vanmaekelbergh, D. & Delerue, C. Electronic structure of atomically coherent square semiconductor superlattices with dimensionality below two. *Phys. Rev. B* **88**, 115431 (2013).

11. Kalesaki, E. *et al.* Dirac Cones, Topological Edge States, and Nontrivial Flat Bands in Two-Dimensional Semiconductors with a Honeycomb Nanogeometry. *Phys. Rev. X* **4**, 011010 (2014).

12. Beugeling, W. *et al.* Topological states in multi-orbital HgTe honeycomb lattices. *Nat. Commun.* **6**, 6316 (2015).

13. Evers, W. H. *et al.* High charge mobility in two-dimensional percolative networks of PbSe quantum dots connected by atomic bonds. *Nat. Commun.* **6,** 8195 (2015).

14. Pietra, F. *et al.* Semiconductor nanorod self-assembly at the liquid/air interface studied by in situ GISAXS and ex situ TEM. *Nano Lett.* **12**, 5515–5523 (2012).

15. Bian, K. *et al.* Shape-anisotropy driven symmetry transformations in nanocrystal superlattice polymorphs. *ACS Nano* **5**, 2815–2823 (2011).

16. Li, R., Bian, K., Hanrath, T., Bassett, W. A. & Wang, Z. Decoding the superlattice and interface structure of truncate PbS nanocrystal-assembled supercrystal and associated interaction forces. *J. Am. Chem. Soc.* **136**, 12047–12055 (2014).

17. Choi, J. J. *et al.* Controlling nanocrystal superlattice symmetry and shape-anisotropic interactions through variable ligand surface coverage. *J. Am. Chem. Soc.* **133**, 3131–3138 (2011).

18. Choi, J. J., Bian, K., Baumgardner, W. J., Smilgies, D.-M. & Hanrath, T. Interface-induced nucleation, orientational alignment and symmetry transformations in nanocube superlattices. *Nano Lett.* **12,** 4791–8 (2012).

19. Evers, W. H. *et al.* Entropy-driven formation of binary semiconductor-nanocrystal superlattices. *Nano Lett.* **10,** 4235–4241 (2010).

20. Bodnarchuk, M. I., Kovalenko, M. V, Heiss, W. & Talapin, D. V. Energetic and entropic contributions to self-assembly of binary nanocrystal superlattices: temperature as the structure-directing factor. *J. Am. Chem. Soc.* **132,** 11967–11977 (2010).

21. Hanrath, T., Choi, J. J. & Smilgies, D.-M. Structure/processing relationships of highly ordered lead salt nanocrystal superlattices. *ACS Nano* **3,** 2975–88 (2009).

22. Narayanan, S., Wang, J. & Lin, X.-M. Dynamical self-assembly of nanocrystal superlattices during colloidal droplet evaporation by in situ small angle x-ray scattering. *Phys. Rev. Lett.* **93,** 135503 (2004).

23. Woo, J. Y. *et al.* Ultrastable PbSe Nanocrystal Quantum Dots via in Situ Formation of Atomically Thin Halide Adlayers on PbSe(100). *J. Am. Chem. Soc.* **136**, 8883-8886 (2014).

24. Van Aert, S., Batenburg, K. J., Rossell, M. D., Erni, R. & Van Tendeloo, G. Three-dimensional atomic imaging of crystalline nanoparticles. *Nature* **470,** 374–347 (2011).

25. Van Aert, S. *et al.* Procedure to count atoms with trustworthy single-atom sensitivity. *Phys. Rev. B* **87,** 064107 (2013).

26. Jones, L., MacArthur, K. E., Fauske, V. T., van Helvoort, A. T. J. & Nellist, P. D. Rapid estimation of catalyst nanoparticle morphology and atomic-coordination by high-resolution Z-contrast electron microscopy. *Nano Lett.* **14,** 6336–6341 (2014).

27. Bals, S. *et al.* Atomic scale dynamics of ultrasmall germanium clusters. *Nat. Commun.* **3,** 897 (2012).

28. Simon, P. *et al.* Interconnection of nanoparticles within 2D superlattices of PbS/oleic acid thin films. *Adv. Mater.* **26**, 3042–3049 (2014).

29. Sandeep, C. S. S. *et al.* Epitaxially connected PbSe quantum-dot films: controlled neck formation and optoelectronic properties. *ACS Nano* **8**, 11499–11511 (2014).

30. Baumgardner, W. J., Whitham, K. & Hanrath, T. Confined-but-connected quantum solids via controlled ligand displacement. *Nano Lett.* **13,** 3225–3231 (2013).

31. Zhang, H., De Yoreo, J. J. & Banfield, J. F. A Unified Description of Attachment-Based Crystal Growth. *ACS Nano* **8**, 6526,6530 (2014).

32. Zhang, H. & Banfield, J. F. Energy Calculations Predict Nanoparticle Attachment Orientations and Asymmetric Crystal Formation. *J. Phys. Chem. Lett.* **3**, 2882–2886 (2012).

33. Steckel, J. S., Yen, B. K. H., Oertel, D. C. & Bawendi, M. G. On the mechanism of lead chalcogenide nanocrystal formation. *J. Am. Chem. Soc.* **128**, 13032–13033 (2006).

34. Whitham, K. *et al.* Charge transport and localization in atomically coherent quantum dot solids. *Nat. Mater.* **15,** 557–563 (2016).

35. During the review of this article, the self-assembly and atomic alignment of PbS nanocrystals into large 3D superstructures was studied, which show a FCC to BCC phase transition: Weidman, M. C., Smilgies, D.-M. & Tisdale, W. A. Kinetics of the self-assembly of nanocrystal superlattices measured by real-time in situ X-ray scattering. *Nat. Mater.* (2016). doi:10.1038/nmat4600